

# Progress on slip wall modeled LES for predicting smooth body separation

By M. P. Whitmore, S. T. Bose<sup>†</sup> AND P. Moin

## 1. Motivation and objectives

The use of large-eddy simulation (LES) as a tool for engineering design has begun to grow in the last decade as advances in computational resources have made it possible to efficiently simulate increasingly complex flows and geometries in realistic conditions. The promise of LES, in comparison to Reynolds-averaged Navier-Stokes (RANS) simulation, is that by resolving the large, energy-containing scales of the flow and modeling the more universal small scales, LES is capable of providing accurate and predictive results that do not require significant tuning of coefficients. The predictive nature of LES is important in furthering the goal of certification by analysis, whereby aircraft designers can certify new aircraft through a combination of numerical simulations and wind tunnel experiments, reducing the need for expensive flight tests and accelerating the design process (Goc 2023). While existing computational fluid dynamics methods are well calibrated to simulate aircraft cruise conditions, LES could be used to better understand aircraft behavior near the corners of the flight envelope, such as near stall boundaries in high-lift configurations or near buffet boundaries. These flows are difficult to simulate and model because they contain many complex flow phenomena such as pressure gradient effects, separated turbulent boundary layers, and shock boundary layer interactions. The focus of this work is on pressure gradient effects and smooth body separation of turbulent boundary layers, which is relevant especially to the high-lift aircraft configuration that is used during takeoff and landing.

When dealing with wall-bounded turbulent flows, two types of LES can be used. Because the large, energy-containing scales of turbulence in boundary layers scale with the distance to the wall, the computational mesh used must be refined significantly near the wall in order to resolve the large scales there (Townsend 1976). This approach, called wall-resolved LES, is accurate but often comes with an intractable computational cost as the Reynolds number increases (Yang & Griffin 2021; Choi & Moin 2012). The other approach is to maintain a constant grid spacing near the wall. A wall model is then introduced in order to represent the behavior of the unresolved near-wall flow and impose its effect onto the outer LES. This approach, called wall-modeled LES (WMLES), allows for affordable computation of high-Reynolds-number flows because there is no requirement to resolve the smallest scales in the inner layer of the boundary layer.

Traditional wall models for LES rely on the assumption of a thin boundary layer, typically in dynamical equilibrium, such that the law of the wall may be directly imposed either through solution fitting or through a RANS-based eddy viscosity (Cabot & Moin 2000). These assumptions break down in the presence of strong non-equilibrium effects like pressure gradients, as well in the vicinity of complex flow features such as separation; however these are the scenarios that we are most interested in predicting

<sup>†</sup> Cascade Technologies, Palo Alto, CA

with WMLES. An alternative wall-modeling methodology is slip wall modeling, which represents the effect of the near-wall flow through a slip velocity on the wall. The slip wall boundary condition itself is rigorously derived and makes no assumptions about the flow. This methodology then requires the modeling of a slip length at the wall, rather than directly modeling the wall shear stress. The slip wall model is expected to provide improved predictive capabilities especially in the complex non-equilibrium flow regimes where traditional wall models are known to fail. This is because it does not rely on a thin boundary layer assumption or dynamical equilibrium as many wall-stress models do. In order to develop and validate the predictive capabilities of slip wall modeling for complex flow phenomena, we simulate the flow around the Boeing speed bump, which involves turbulent smooth body separation as well as strong pressure gradient effects (Williams *et al.* 2020; Gray *et al.* 2021).

This study builds upon the previous study by Whitmore *et al.* (2021). In particular, we are interested in investigating the effects of improved inflow turbulence, as well as investigating the grid convergence properties of previously studied wall models. In this brief, we first discuss the modeling framework to be used. Then we introduce the flow configuration, followed by description of the inlet conditions. Finally we present the WMLES results and offer some conclusions.

## 2. Modeling framework

The governing equations for LES are derived by applying a low-pass filter to the Navier-Stokes equations, such that, for an incompressible fluid

$$\bar{u}_i(x) = \int G(x', x; \Delta) u_i(x') dx', \quad (2.1)$$

$$\frac{\partial \bar{u}}{\partial t} + \frac{\partial}{\partial x_j} (\bar{u}_i \bar{u}_j) = \frac{1}{\rho} \frac{\partial \bar{p}}{\partial x_i} - \frac{\partial \tau_{ij}}{\partial x_j} + \nu \frac{\partial^2 \bar{u}_i}{\partial x_j \partial x_j}; \quad \frac{\partial \bar{u}_k}{\partial x_k} = 0, \quad (2.2)$$

where  $G$  is the low-pass filter kernel,  $\bar{u}_i$  is the filtered velocity field,  $\bar{p}$  is the filtered pressure field,  $\nu$  is the molecular kinematic viscosity,  $\rho$  is the fluid density, and the subgrid-stress tensor  $\tau_{ij} = \overline{u_i u_j} - \bar{u}_i \bar{u}_j$  is an unclosed term. No assumption was made about the filter kernel  $G$  except that the filter operation commutes with differentiation. Additionally, we note that the filter kernel  $G$  is assumed to depend parametrically on the numerical grid length scale  $\Delta$ . The subgrid-stress tensor in this brief is modeled with an eddy viscosity model such that the deviatoric part is

$$\tau_{ij} - \frac{\tau_{kk}}{3} \delta_{ij} \approx -2\nu_t \bar{S}_{ij}, \quad (2.3)$$

where  $\nu_t$  is the eddy viscosity, and  $\bar{S}_{ij}$  is the filtered rate-of-strain tensor. The isotropic part  $\tau_{kk}$  is included in the pressure term and therefore is not explicitly modeled. In this brief, the eddy viscosity  $\nu_t$  is modeled using the dynamic Smagorinsky model (Germano *et al.* 1991; Lilly 1992).

Now the governing equations are nearly closed, except that the boundary conditions still need to be specified. Specifically, we need to choose boundary conditions for the filtered velocity field in the presence of a solid wall. The underlying Navier-Stokes solution at a solid wall obeys a no-slip and no-penetration condition such that  $u_i|_w = 0$ , where  $(\cdot)|_w$  denotes evaluation at the wall. The filtered velocity field  $\bar{u}_i$  is not expected to obey the no-slip/no-penetration boundary condition, except in the asymptotic limit

of wall-resolved LES (Bose & Moin 2014). Instead, we must introduce a model boundary condition for the filtered velocity field. Given a choice of filter kernel  $G$ , it would be possible to derive a corresponding boundary condition for the filtered velocity field. However, here we do not prescribe a filter explicitly; therefore, there are multiple possible options for boundary conditions for the field  $\bar{u}_i(x_j)$ . As shown by Bose & Moin (2014), assuming a top hat box filter leads to finite-volume-type scheme where the wall is represented as a wall-stress flux. This can be represented as a traditional wall-stress boundary condition (Cabot & Moin 2000), wherein we choose a Neumann velocity condition to impose the desired wall stress, such that

$$\nu \frac{\partial \bar{u}_t}{\partial n} \Big|_w = \tau_w; \quad \bar{u}_n|_w = 0, \quad (2.4)$$

where  $t$  denotes the wall-tangential direction,  $n$  denotes the wall-normal direction, and  $\tau_w$  is the wall shear stress that is given by a wall-stress model. Given this boundary condition, it is necessary to provide a model for the wall shear stress  $\tau_w$ . In this brief, this is done through the use of an algebraic equilibrium wall-stress model (EQWM). We use a piecewise  $C^1$ -continuous fit for the law of the wall (Lehmkuhl *et al.* 2018), which is then iteratively used to compute a wall stress by matching to the LES velocity at the first control volume off the wall.

Alternatively, by assuming a differential filter, Bose & Moin (2014) derived the slip boundary condition, where we set a Robin condition

$$\bar{u}_i|_w = (C\Delta_w) \frac{\partial \bar{u}_i}{\partial n} \Big|_w, \quad (2.5)$$

which introduces a finite slip velocity on the wall, including a transpiring component, and where the slip length  $C\Delta_w$  is specified with the wall-normal distance to the wall  $\Delta_w$  and a non-dimensional coefficient  $C$ . In this brief, the slip length model that is used is a static model with the form

$$C\Delta_w = \kappa\Delta_w [1 - \exp(-\Delta_w^+/A^+)] \approx \ell_m, \quad (2.6)$$

where  $\kappa = 0.41$  is the von Kármán constant,  $A^+$  is a damping constant, and  $\ell_m$  is written to emphasize that this model resembles a mixing length model for the slip length. In this brief, the value of  $A^+$  is taken to be 17. This model is the same as the one presented by Whitmore *et al.* (2021). Note that the slip wall model, in contrast to the EQWM, generates a wall stress through the resolved Reynolds stresses at the wall. Therefore, it is expected that the slip wall model will be more sensitive to the quality of the resolved turbulence in the calculation. Additionally, because the slip wall model is generating a resolved Reynolds shear stress at the wall, it could be appropriate to introduce a subgrid-scale model on the wall; however, this is not explored in this brief.

### 3. Flow configuration

The flow we study in this brief is the Boeing speed bump, otherwise known as the smooth body separation experiment, which is intended as a canonical case of turbulent smooth body separation. This analytically defined geometry was proposed by the Boeing Company and studied in collaboration with experimental groups at the University of Washington (Williams *et al.* 2020) and the University of Notre Dame (Gray *et al.* 2021). A spanwise-periodic section of the geometry has also been the subject of a high-fidelity

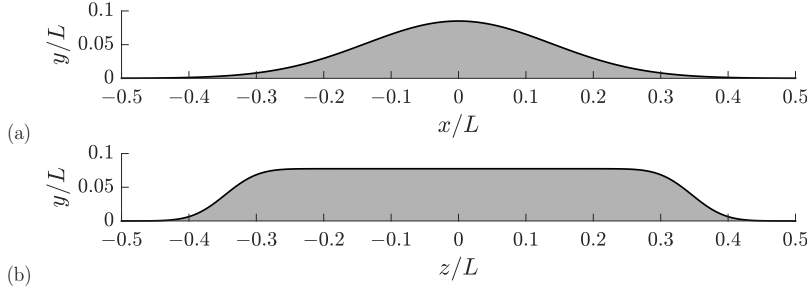


FIGURE 1. Cross sections of the bump geometry showing (a) a slice along the centerline ( $z/L = 0$ ) and (b) a slice along the span ( $x/L = 0$ ). The geometry has side walls at  $z/L = \pm 0.5$  and a top wall at  $y/L = 0.5$ .

quasi-direct numerical simulation by Uzun & Malik (2022). The geometry is analytically defined as

$$f(x, z) = \frac{h}{2} e^{-(x/x_0)^2} \left\{ 1 + \operatorname{erf} \left[ \left( \frac{L}{2} - 2z_0 - |z| \right) / z_0 \right] \right\}, \quad (3.1)$$

where  $f$  is the surface of the bump, and  $x$  and  $z$  are the axial and spanwise coordinates in the wind tunnel, respectively. The length scale  $L$  denotes the width of the bump and is used for non-dimensionalization. The other parameters are set as  $h = 0.085L$ , the height of the bump apex, and as  $x_0 = 0.195L$  and  $z_0 = 0.06L$ , length scales governing the axial and spanwise variation, respectively. Cross sections of the geometry are shown in Figure 1. The spanwise-periodic configuration is an extrusion of the centerline cross section,  $f(x, 0)$ , with a width of  $L_z = 0.08L$  to allow an affordable high-fidelity simulation (Uzun & Malik 2022). In this brief, we focus primarily on the spanwise-periodic configuration. As observed by Whitmore *et al.* (2021), the spanwise-periodic section exhibits similar flow behavior to the experimental configuration along the centerline.

The characteristic Reynolds number for this geometry,  $Re_L = \rho_\infty U_\infty L / \mu_\infty$ , where  $U_\infty$  is the freestream velocity, was in the range of  $O(1.8 \times 10^6 - 4 \times 10^6)$  for the experimental campaigns. The spanwise-periodic case is conducted at a lower Reynolds number of  $Re_L = 2 \times 10^6$ . The freestream Mach number is low,  $Ma = 0.2$ , such that no compressibility effects are expected. Despite the low Mach number, we use a compressible solver for convenience.

The quantities of interest for this flow are the pressure coefficient  $C_p$  and skin-friction coefficient  $C_f$ . These quantities are defined as

$$C_p \equiv \frac{p_w - p_{ref}}{\frac{1}{2} \rho_\infty U_\infty^2} \quad \text{and} \quad C_f \equiv \frac{\tau_w}{\frac{1}{2} \rho_\infty U_\infty^2}, \quad (3.2)$$

where  $p_w$  and  $\tau_w$  denote the mean wall pressure and wall shear stress, respectively. The reference pressure  $p_{ref}$  is taken to be the centerline wall pressure at  $x/L = -0.83$ , similar to Williams *et al.* (2020). Data from Uzun & Malik (2022) are used as reference for both quantities of interest.

The flow solver used in this brief is charLES, a compressible unstructured finite-volume solver with low dissipation numerics (Brès *et al.* 2018). The code uses arbitrary polyhedral meshes based on Voronoi diagrams generated with hexagonally close-packed point seeding. Grid refinement is done via homothetic refinement of the grid cells in layers near the wall, in order to resolve the outer layer of the boundary layer. Details of the computational mesh resolutions used in this brief are given in Table 1. Note that the

Mesh	$N_{CV}$	$\max \Delta/L$	$\min \Delta/L$	$\min \Delta/\delta_0$	$\max_{x<0} y_1^+$	$\min_{x<0} y_1^+$
Coarse	3.7 mil.	0.01	$1.3 \times 10^{-3}$	0.16	62	31
Medium	14 mil.	0.01	$6.3 \times 10^{-4}$	0.08	30	16
Fine	57 mil.	0.01	$3.1 \times 10^{-4}$	0.04	14	8
Very Fine	225 mil.	0.01	$1.5 \times 10^{-4}$	0.02	9	4

TABLE 1. Mesh parameters for the spanwise-periodic configuration at  $Re_L = 2 \times 10^6$ . The quantity  $y_1^+$  is the span-averaged distance of the first control volume center from the wall in inner units, computed from the EQWM case.

ranges of resolutions in inner units,  $y_1^+$ , express the size of the half-height of the cell, so the cells are at least a factor of two larger. Additionally, while the finest grid resolution does appear to be extremely fine in inner units, the results are still poor when a wall model is not used, and it is expected that these grids are still a few levels of refinement away from adequate wall-resolved LES resolution.

A freestream parallel velocity is imposed at the top boundary. A non-reflective characteristic outflow condition is used at the end of the domain. The domain extent is  $x/L \in [-1, 2.5]$  for the recycling and rescaling inlet and  $x/L \in [-1.5, 2.5]$  for the synthetically tripped inlet. The wall boundary conditions were discussed in the previous section. The inflow boundary conditions are detailed in the next section.

#### 4. Inflow conditions

The inflow conditions detailed herein are specifically intended as methods for the generation of turbulent fluctuations inside the incoming boundary layer. Both methods can be used in conjunction with a specified mean velocity profile at the inlet plane. For the spanwise-periodic configuration of the bump we impose a mean velocity profile to match that of Uzun & Malik (2022).

Both of the following inflow conditions are presented here as higher-fidelity methods than were used in the previous study by Whitmore *et al.* (2021). In that study, the inflow condition was a simple quiescent inflow profile which relied on the growth of numerical errors to induce the transition to turbulence.

##### 4.1. Synthetic tripping

The method for synthetic tripping of the inflow used in this brief relies on the imposition of a blowing and suction strip on the wall near the inflow boundary. At the inflow boundary, a quiescent velocity profile is sent into the domain. The boundary condition imposed on the wall in the tripping strip has the form

$$\bar{u}_t = 0; \quad \bar{u}_n = u_c \sin(2\pi ft), \quad (4.1)$$

where  $u_c$  is a velocity amplitude chosen to be  $O(5\%)$  of the freestream velocity  $U_\infty$ , which also happens to be  $O(u_\tau)$  at the inlet. This boundary condition is essentially no-slip with periodic zero-mean transpiration. The frequency  $f$  is chosen such that the non-dimensional frequency is loosely in the range of unstable frequencies for a Blasius boundary layer at the relevant Reynolds number. However, despite this imprecision, the coarsely resolved flow in this case is quite unstable and receptive to a range of

disturbances, so there is little sensitivity to the frequency. Additionally, there was not much sensitivity observed across the range of amplitudes  $O(1-20\%)$  of  $U_\infty$ . When using this method of inflow generation, we shift the inflow location upstream because we expect a longer development length for the boundary layer to become fully turbulent. This behavior was observed during the course of this study but is not explored in depth here.

#### 4.2. Recycled and rescaled inflow turbulence

The recycling and rescaling approach for generating inflow turbulence that is used here is modeled after the work of Lund *et al.* (1998). The velocity that is imposed on the inflow boundary consists of a mean velocity profile with superposed fluctuations

$$\bar{u}_i(x_i^{in}, t) = U_i \left( \frac{x_2}{\delta} \right) + \bar{u}_i^{t*}(x_i^{in}), \quad (4.2)$$

where  $x_i^{in}$  is in the set of points on the inflow boundary,  $U_i$  is an imposed mean profile, and  $\bar{u}_i^{t*}$  are the superposed fluctuating velocities. The fluctuating velocities are defined by

$$\bar{u}_i^{t*}(x_i^{in}) = r_u [\bar{u}_i(x_i^{re}) - \langle \bar{u}_i(x_i^{re}) \rangle], \quad (4.3)$$

where  $x_i^{re}$  is in the set of points on the chosen recycling plane, which will be defined by a one-to-one mapping of the set of points on the inflow boundary,  $\langle \cdot \rangle$  denotes a temporal average, and  $r_u$  denotes a scaling factor that is used to appropriately rescale the velocity fluctuations to match the desired inflow conditions. The mapping  $f: \mathbb{R}^3 \rightarrow \mathbb{R}^3$  is defined by

$$f(x_i) \equiv \left( x_1 + \Delta_1, \frac{\delta(f(x_i))}{\delta(x_i)} x_2, x_3 + \Delta_3 \right), \quad (4.4)$$

where  $\delta(\cdot)$  returns the 99% boundary layer thickness at that streamwise location, and we let  $x_i^{re} = f(x_i^{in})$ . Note this map is valid only inside the boundary layer; however, we do not need to do recycling in the freestream. Also note that this definition is implicit as it requires knowledge of the boundary layer thickness at the upstream recycling plane. However, the flow is steady, so the boundary layer thickness will not vary, particularly in attached flow. In order to save on computational cost, we use an empirical power law relating  $\delta/x \sim Re_x^{-1/6}$ , as discussed by Wu (2017). The streamwise offset is  $\Delta_1 = 0.5L$  and the spanwise offset is  $\Delta_3 = L_z/2$ . This spanwise offset is done, similar to Spalart *et al.* (2006), to allow the recycling plane to be moved closer to the inlet plane without having strong coupling of the flow structures. The factor  $r_u$  is set to  $u_\tau(x_i^{in})/u_\tau(x_i^{re})$ , which can also be estimated from an empirical  $C_f \sim Re^{-1/6}$  power law scaling. Note also that this procedure does not use the inner layer scaling outlined by Lund *et al.* (1998) because the grids are coarse, and additionally the inner layer scales are fast and should recover more quickly. An improved approach may take the inner layer scaling into account, as well as dynamically compute the boundary layer thickness; however, this procedure was determined to be adequate for the WMLES in this brief.

## 5. Results for the spanwise-periodic bump

The simulations of the spanwise-periodic configuration are carried out at  $Re_L = 2 \times 10^6$ . First we conduct the simulations with the synthetic tripping method for turbulent inflow generation. The results for the pressure coefficient with the two wall models are shown in Figure 2, and the results for the skin-friction coefficient are shown in Figure 3. Figure 2(a) demonstrates that, in the separation region marked by the flattened region of  $C_p$ ,

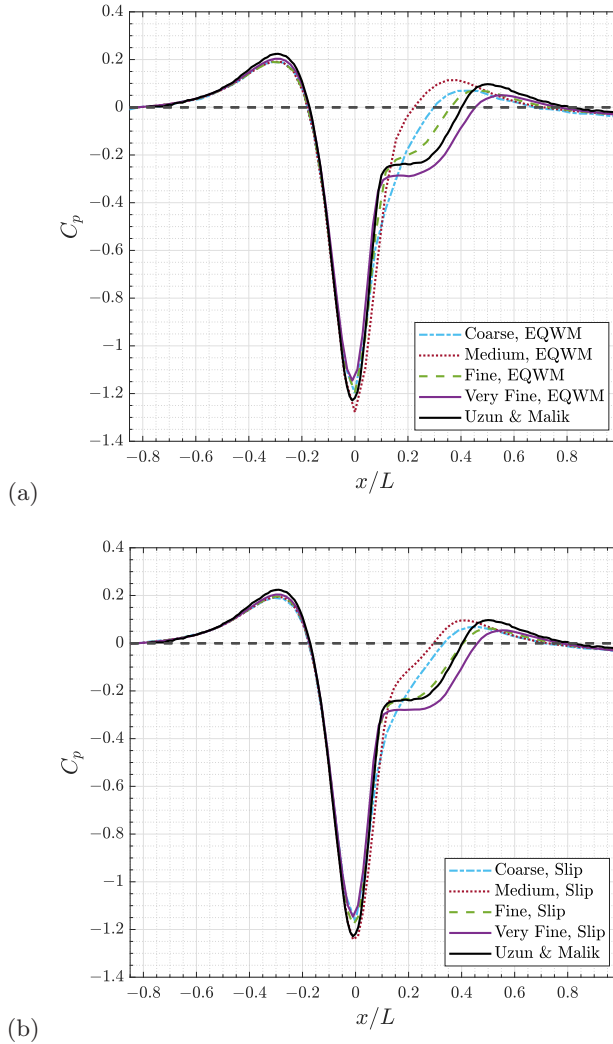


FIGURE 2. Pressure coefficient results for the spanwise-periodic configuration at  $Re_L = 2 \times 10^6$  using (a) the EQWM and (b) the slip wall model. Both cases use the synthetic tripping method for turbulent inflow generation.

the EQWM predicts a slight flattening of the pressure coefficient on the coarse grid. The flattening diminishes on the medium grid as the flow remains attached, but on the fine and very fine grids the separation bubble is recovered, becoming accurate on the very fine grid. Figure 2(b) shows that the slip wall model expresses similar behavior, with a slightly more accurate result on the medium grid, and then agrees well with the reference data on the fine grid.

The behavior of the separation bubble is clearer in Figure 3, where the EQWM does not predict any region of mean negative skin friction on the medium grid, while the slip wall model predicts a mean separation bubble on all grids, albeit with underpredicted size on the medium grid, but ultimately becomes accurate in the separation bubble on the fine and very fine grids. Looking at the upstream region as well as in the reattachment

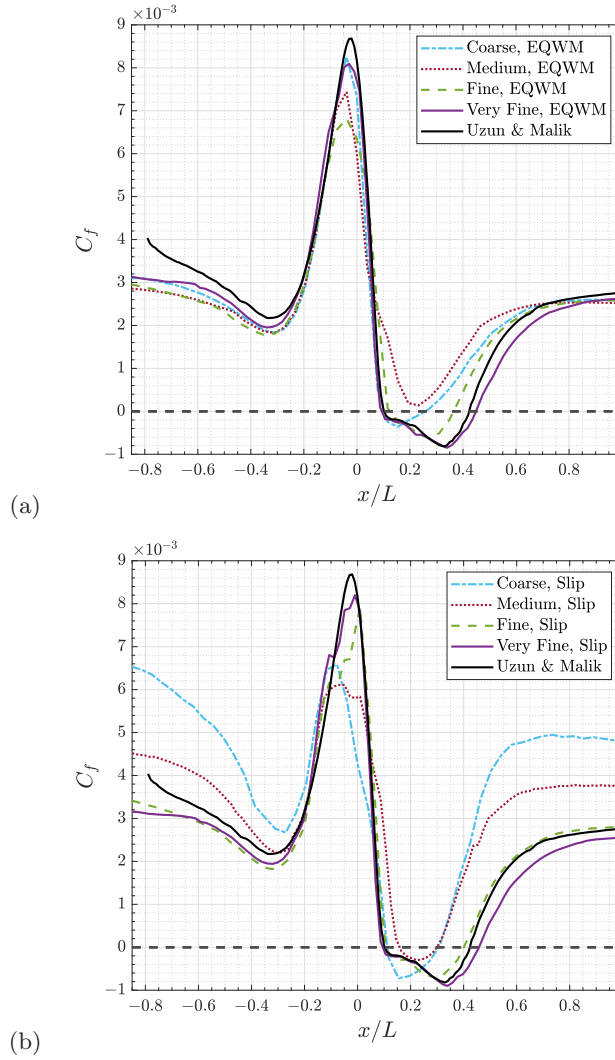


FIGURE 3. Skin-friction coefficient results for the spanwise-periodic configuration at  $Re_L = 2 \times 10^6$  using (a) the EQWM and (b) the slip wall model. Both cases use the synthetic tripping method for turbulent inflow generation.

and recovery regions, we notice that the slip wall model is overpredicting the skin friction on coarse grids, especially compared to the EQWM. This is not surprising because the static slip wall model used in this brief is not designed to encode the flat plate behavior the way the EQWM is designed, and signifies an area of improvement for the slip wall model. However, the slip wall model exhibits grid-convergence behavior on finer grids, as well as better predictions of the separation bubble across grid resolutions.

Note that in the upstream region, with both wall models, the results on the fine and very fine grids are not converging to the reference skin-friction data. This is due to the handling of the inflow condition. For this reason, we wish to look at the results when using the improved inflow condition with recycling and rescaling for generation of inflow turbulence. We are particularly interested in doing so in order to determine the sensitivity

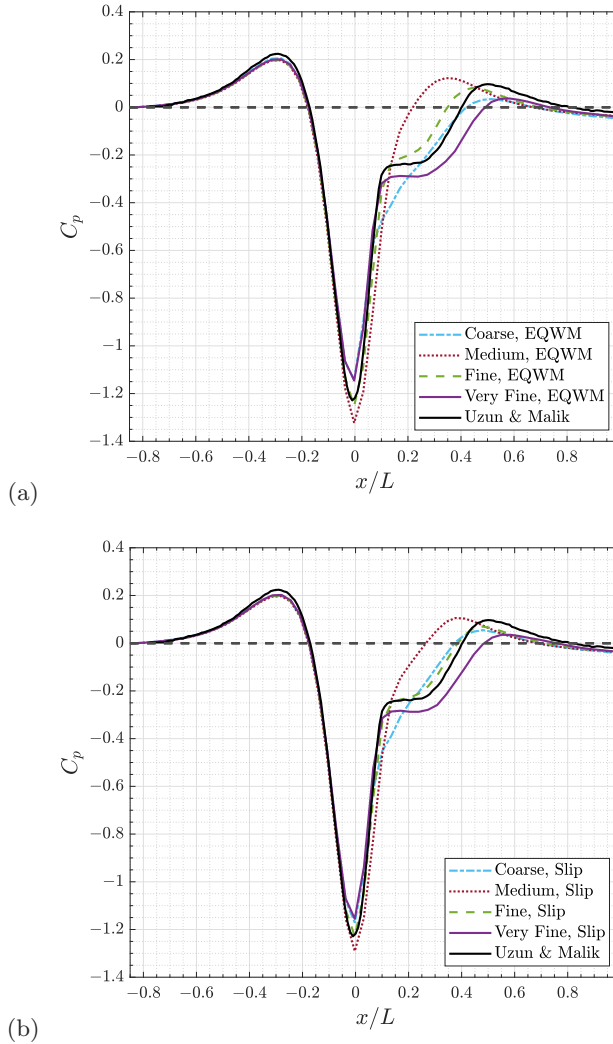


FIGURE 4. Pressure coefficient results for the spanwise-periodic configuration at  $Re_L = 2 \times 10^6$  using (a) the EQWM and (b) the slip wall model. Both cases use the recycling and rescaling method for turbulent inflow generation.

of the wall-modeling approaches to the inflow conditions. Specifically, we expect that the slip wall model will be sensitive to the quality of the boundary layer inflow turbulence because the slip wall model generates wall stress through a resolved Reynolds stress at the wall that depends on the fluctuations resolved by the calculation. In contrast, the EQWM directly imposes the zero-pressure-gradient flat plate turbulent boundary layer behavior and should be relatively less sensitive to the quality of the inflow turbulence.

The results for the pressure coefficient and skin-friction coefficient for the simulations using the recycling and rescaling method for turbulent inflow generation are shown in Figures 4 and 5, respectively. Figure 4(a) shows similar behavior for the EQWM, except that in the upstream region the results, particularly on the finer grids, have improved agreement with the reference data.

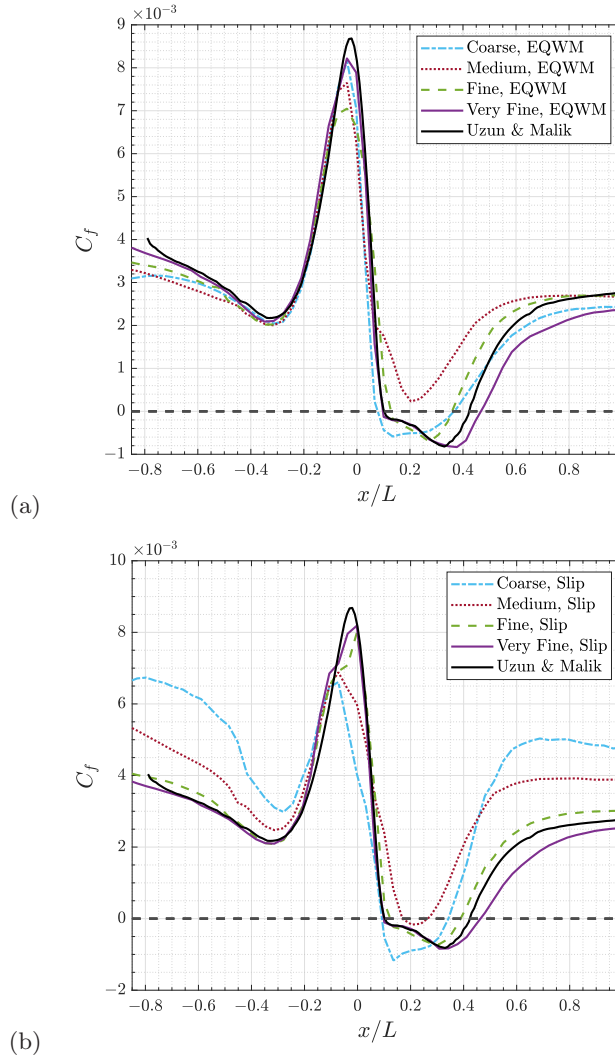


FIGURE 5. Skin-friction coefficient results for the spanwise-periodic configuration at  $Re_L = 2 \times 10^6$  using (a) the EQWM and (b) the slip wall model. Both cases use the recycling and rescaling method for turbulent inflow generation.

Figure 5(b) shows that the slip wall model maintains a generally improved prediction of the separation bubble compared to the EQWM and has similar accuracy inside the separation bubble compared to the previous slip wall model result with the synthetically tripped inflow condition. The slip wall model results show reasonably grid-converged results across the fine and very fine grids. On both grids, the separation bubble is predicted with relative accuracy, but the upstream skin friction shows particularly good agreement with the reference data. In addition, the prediction of the peak skin friction is in good agreement with the reference data on the very fine grid.

Finally, we note that the results, particularly for the slip wall model, for both inflow conditions demonstrate significant improvement over the results previously shown by Whitmore *et al.* (2021). Specifically, the previous results had seen larger over-prediction

of the upstream skin friction, as well as worse agreement of the upstream skin friction and peak skin friction, particularly on the fine grid resolution. Additionally, the new results on the very fine grid show that the results with the slip wall model are indeed reaching an approximately grid-converged state and that the agreement with the reference data is not fortuitous. We note that, in comparison to the results obtained by Whitmore *et al.* (2021), the separation bubble predicted by the slip wall model on the medium grid here is somewhat diminished, particularly compared to size of the bubble on the coarse grid. This is likely due to changes made in the numerical operators of the code to improve kinetic energy conservation. The behavior is not currently well understood, but it is expected that an improved slip wall model can be made robust to the effect.

## 6. Conclusions

In this brief we have detailed efforts to develop new wall modeling methodologies that can be used to provide improved predictions of turbulent smooth body separation. This was done through simulations of the Boeing speed bump, which is regarded as a canonical case of smooth body separation. Specifically, simulations of the spanwise-periodic section of the Boeing speed bump geometry were shown. First, two different wall modeling strategies were detailed, namely equilibrium wall modeling and slip wall modeling. Then, we discussed two different methods for generating higher-fidelity inflow turbulence. These methods were synthetic tripping of the boundary layer through a blowing and suction boundary condition and a recycling and rescaling procedure adapted from Lund *et al.* (1998).

The results with the slip wall model gave improved predictions of the separation bubble across grid resolutions, as compared to the EQWM. This was in agreement with the previous results of Whitmore *et al.* (2021). In both cases of the improved inflow conditions, the results demonstrated improvements over the previous results of Whitmore *et al.* (2021), especially in the upstream flat plate region, as well as around the skin-friction peak. Between the two inflow turbulence generation methods, the recycling and rescaling procedure gave results in better agreement with the reference data and required a shorter development length for the incoming boundary layer to become fully turbulent.

## Acknowledgments

This investigation was funded by NASA Transformational Tools and Technologies grant #80NSSC20M0201. Computational resources were provided by Oak Ridge Leadership Computing Facility.

## REFERENCES

- BOSE, S. T. & MOIN, P. 2014 A dynamic slip boundary condition for wall-modeled large-eddy simulation. *Phys. Fluids* **26**, 015104.
- BRÈS, G. A., BOSE, S. T., EMORY, M., HAM, F. E., SCHMIDT, O. T., RIGAS, G. & COLONIUS, T. 2018 Large-eddy simulations of co-annular turbulent jet using a Voronoi-based mesh generation framework. *AIAA Paper* 2018-3302.
- CABOT, W. H. & MOIN, P. 2000 Approximate wall boundary conditions in the large-eddy simulation of high Reynolds number flow. *Flow Turbul. Combust.* **63**, 269–291.

- CHOI, H. & MOIN, P. 2012 Grid-point requirements for large eddy simulation: Chapman's estimates revisited. *Phys. Fluids* **24**, 30–35.
- GERMANO, M., PIOMELLI, U., MOIN, P. & CABOT, W. H. 1991 A dynamic subgrid-scale eddy viscosity model. *Phys. Fluids A-Fluid* **3**, 1760–1765.
- GOC, K. A. 2023 Towards certification by analysis: large eddy simulations of commercial aircraft across the flight envelope. PhD thesis, Stanford University.
- GRAY, P. D., GLUZMAN, I., THOMAS, F., CORKE, T., LAKEBRINK, M. & MEJIA, K. 2021 A new validation experiment for smooth-body separation. *AIAA Paper* 2021-2810.
- LEHMKUHL, O., PARK, G. I., BOSE, S. T. & MOIN, P. 2018 Large-eddy simulation of practical aeronautical flows at stall conditions. *Proceedings of the Summer Program*, Center for Turbulence Research, Stanford University, pp. 87–96.
- LILLY, D. K. 1992 A proposed modification of the Germano subgrid-scale closure method. *Phys. Fluids A-Fluid* **4**, 633–635.
- LUND, T. S., WU, X. & SQUIRES, K. 1998 On the generation of turbulent inflow conditions for boundary layer simulations. *J. Comput. Phys.* **140**, 233–258.
- SPALART, P. R., STRELETS, M. & TRAVIN, A. 2006 Direct numerical simulation of large-eddy-break-up devices in a boundary layer. *Int. J. Heat Fluid Fl.* **27**, 902–910.
- TOWNSEND, A. A. 1976 *The Structure of Turbulent Shear Flow*. 2nd ed. Cambridge University Press.
- UZUN, A. & MALIK, M. R. 2022 High-fidelity simulation of turbulent flow past Gaussian bump. *AIAA J.* **60**, 2130–2149.
- WHITMORE, M. P., GRIFFIN, K. P., BOSE, S. T. & MOIN, P. 2021 Large-eddy simulation of a Gaussian bump with slip-wall boundary conditions. *Annual Research Briefs*, Center for Turbulence Research, Stanford University, pp. 45–58.
- WILLIAMS, O., SAMUEL, M., SARWAS, S., ROBBINS, M. & FERRANTE, A. 2020 Experimental study of a CFD validation test case for turbulent separated flows. *AIAA Paper* 2020-0092.
- WU, X. 2017 Inflow turbulence generation methods. *Ann. Rev. Fluid Mech.* **49**, 23–49.
- YANG, X. I. A. & GRIFFIN, K. P. 2021 Grid-point and time-step requirements for direct numerical simulation and large-eddy simulation. *Phys. Fluids* **33**, 015108.